Front. Struct. Civ. Eng. 2025, 19(5): 742–759
https://doi.org/10.1007/s11709-025-1179-2

RESEARCH ARTICLE

Investigation of deformation mechanisms in intersecting sections of interchange tunnels using the negative Poisson's ratio anchor excavation compensation method

Songyuan LIU[a,b], Yadong MAO[a,b], Zhifeng DU[a,b], Liang GAO[c], Shiding CAO[a,b,d], Manchao HE[a,b], Zhigang TAO[a,b*]

[a] *School of Mechanics and Civil Engineering, China University of Mining and Technology, Beijing 100083, China*
[b] *State Key Laboratory for Tunnel Engineering, China University of Mining and Technology, Beijing 100083, China*
[c] *Guangzhou Daguang Expressway Co., Ltd., Guangzhou 510900, China*
[d] *Shenzhen Transportation Design & Research Institute Co., Ltd., Shenzhen 518803, China*
[*] *Corresponding author. E-mail: taozhigang@cumtb.edu.cn*

ABSTRACT The study focused on the intersecting section of the Nalong Underground Interchange Tunnel in Shenzhen and investigated the deformation mechanism of the intersecting section under excavation and overloading conditions using physical model tests and numerical simulation methods. First, the optimal similarity ratio was determined based on the tunnel's actual geometric characteristics, spatial distribution, and engineering geological conditions. A physical model of the intersecting section was then established. Secondly, following the excavation compensation theory, the intersecting section was excavated and supported using scaled Negative Poisson's Ratio (NPR) anchor cables. The analysis of tunnel stress−strain, displacement, and NPR anchor cable axial force revealed the stress redistribution characteristics of the tunnel during excavation. Subsequently, the tunnel underwent overloading tests to reveal the surrounding rock failure mechanism of the intersecting section. Finally, numerical simulations were used to compare and verify the test results. The deformation mechanism and damage mode of the similar physical model of the intersecting section of Shenzhen Nanlong Underground Interchange Tunnel under the condition of excavation support and overloading are investigated. The support effect of NPR anchors in the intersection tunnel is verified. The study provides a theoretical basis and practical guidance for the design of tunnel excavation and support with similar engineering background.

KEYWORDS interchange tunnel, excavation compensation method, negative Poisson's ratio anchors, deformation mechanism

1 Introduction

In vibrant urban centers and specialized environments, there is a noticeable increase in the construction of complex interchange tunnel projects [1]. Beijing Subway Line 4 intersects with Line 9 [2]. In the first phase of the Shenzhen Metro project, there is a section from Luohu to Grand Theater where double-deck tunnels overlap vertically [3]. The High Jiulu Road ramp in Chongqing passes over the Daping Tunnel, creating a vertical spatial intersection [4], with a minimum clearance of only 1.685 m. It has become the largest urban underground interchange in China [5].

Several scholars have proposed corresponding construction techniques for specific projects [6–8]. He [9] designed a construction plan for the intersecting section of municipal and rail tunnels and validated its feasibility using FLAC3D. Cheng [10] used numerical simulation to analyze the impact of grouting parameters on surface settlement in the intersection tunnel section. Luo et al.

Article history: Received Sep 9, 2024; Accepted Jan 16, 2025

[11] conducted a study on the effects of blasting construction on the intersection tunnel, combining field monitoring and numerical simulation results. Wang et al. [12] investigated the deformation patterns of surrounding rock in the intersection area of bifurcated tunnels using numerical simulation. Wang et al. [13] studied the impact of a new tunnel passing under an existing tunnel on the surrounding rock of the existing tunnel using numerical simulation. Li and Liu [14] conducted research on zero-spacing construction for deep-buried orthogonal tunnels using Midas-GTS. Xu [15] explored the effects of construction for new tunnels passing underneath existing orthogonal tunnels on surface settlement and the lining structure of existing tunnels using FLAC3D.

The scholars mentioned earlier have primarily concentrated on investigating the mutual influence between two tunnels but have not specifically addressed the support challenges within intersecting tunnels. In the present context, issues related to substantial tunnel deformations are growing in frequency [16,17]. Several scholars have proposed different support methods to solve the problem of large deformation in tunnels. For excavation, the joint blasting method combining directional blasting and non-directional blasting techniques can reduce ground subsidence [18]. He et al. [19] proposed the theory of excavation compensation. Li et al. [20] applied Negative Poisson's Ratio (NPR) anchor cables to tunnel support based on excavation compensation theory. The excavation compensation method has been successfully utilized in the Muzhailing Tunnel [21] and later in soft rock tunnels in Min County [22], Changning [23], and other locations. NPR anchor cables are characterized by high tensile strength, high shear strength and high toughness [24]. While research on NPR anchor cables is extensive [25–28], their effectiveness in supporting intersecting tunnels has yet to be verified.

The effectiveness of tunnel support is often studied using numerical simulations and physical model tests [29]. This paper focuses on the Nalong Underground Interchange Tunnel in Shenzhen, constructing a physical model of the intersecting tunnel based on similarity theory. Physical model tests are conducted on the excavation support and overloading conditions of the intersecting tunnel with NPR anchor reinforcement. After that, numerical simulation is used for verification. The deformation mechanism and damage mode of the similar physical model of the intersecting section of Shenzhen Nanlong Underground Interchange Tunnel under excavation support and overload condition are obtained. The support effect of NPR anchor cables in the interchange tunnel is verified, which provides a theoretical basis and practical guidance for the design of excavation and support of tunnels with similar engineering background.

2 Geological engineering conditions

2.1 Formation lithology and geological structure

The tunnel is located at a depth of 60 m, within an area dominated by moderately weathered, medium-grained granite. This geological formation is known for its distinct joint fractures. During the sampling procedure, it was observed that the surrounding rock exhibited a high degree of fragmentation, with a structural composition consisting of blocky, gravel-like inclusions and blocky configurations. These observations categorize the surrounding rock as falling within the Class IV classification for tunnel support considerations (Fig. 1).

2.2 Initial *in situ* stress

In the deep-buried section of the tunnel, the surrounding rock consists of moderately weathered granite with an R_c standard value of 82 MPa. According to the geological stress test data in the surveyed area, the maximum principal stress $SH < 6$ MPa, $R_c/SH > 10$, indicating a low-stress level. As shown in Table 1, the sampled clasts are hard, but the fractures are relatively well developed. Overall, the likelihood of rock bursts is low.

2.3 Physical and mechanical properties of the surrounding rock

The SC-300 automatic coring machine was utilized to process the standard specimen of the moderately weathered granite sample, while the uniaxial compressive strength and various physical parameters were measured using the 2000 kN indoor uniaxial triaxial system. The results of the uniaxial compression test are shown in Table 2.

Due to the high strength of the surrounding rock and the scarcity of internal fractures, the predominant mode

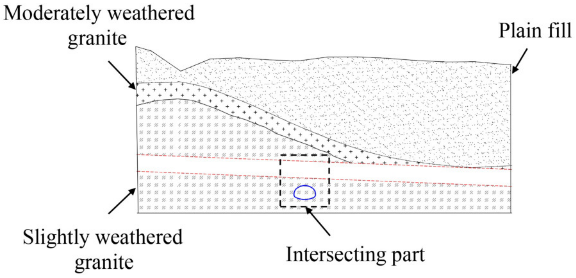

Fig. 1 Schematic diagram of the rock strata around the tunnel.

Table 1 Ratio of *in situ* stress and R_c for the tunnel

No.	Test depth (m)	SH (MPa)	R_c (MPa)	R_c/SH
1	60	< 6	65–75	> 10
2	110	< 6	65–75	> 10

Table 2 Results of the uniaxial compression test

No.	Modulus of elasticity, E (GPa)	Poisson's ratio, μ	Uniaxial compressive strength, σ (MPa)	Failure characteristics
S1	26.5	0.25	93.7	shear
S2	29.0	0.22	90.5	split
S3	27.5	0.24	92.0	split
S4	28.0	0.23	91.8	split
S5	29.0	0.21	91.5	split

of failure is mainly characterized by splitting and fracturing [30].

2.4 Excavation and compensation effect

He et al. [31] introduced the excavation compensation theory as a framework for understanding tunnel excavation processes. This theory dissects the entirety of the excavation process into four distinct phases.

1) Initial stability phase: Before excavation, the rock mass is in a state of equilibrium.

2) Excavation effect 1. Following tunnel excavation, there is a discernible alteration in the stress distribution within the surrounding rock. The radial stress diminishes, ultimately reaching zero.

3) Excavation effect 2. After tunnel excavation, there is a notable concentration of tangential stress, reaching double the original rock stress level. During this phase, the Mohr circle surpasses the Mohr–Coulomb failure envelope. Absent prompt support, the tunnel rock mass is susceptible to failure.

4) High-stress compensation stage: NPR anchors are employed to execute high-stress compensation within the tunnel. The objective is to reinstate the radial stress to its original state to the greatest extent possible. Once radial stress is adequately compensated, the concentration of tangential stress within the rock mass diminishes, and the Mohr circle reverts within the confines of the failure envelope. This stage marks the stabilization of the rock mass (Fig. 2).

2.5 High-stress compensation characteristics of negative Poisson's ratio anchors

The schematic diagram of the NPR anchor structure is shown in Fig. 3. During the anchor's operation, the constant-resistance sleeve remains stationary. Tensile forces are transferred through steel strands to the constant-resistance body, inducing relative slippage between the constant-resistance body and the constant-resistance sleeve. Throughout this phase, the counteracting resistance generated by this slippage remains consistent. Notably, as the constant-resistance body shifts within the constant-resistance sleeve, the sleeve does not contract but rather expands. This design feature guarantees the stability of the NPR anchor's output force throughout its entire operational cycle and safeguards against the risk of anchor failure or fracture during deformation [32].

NPR anchors possess a distinctive structural design that enables them to transmit loads to the constant-resistance body when subjected to tension, effectively preventing

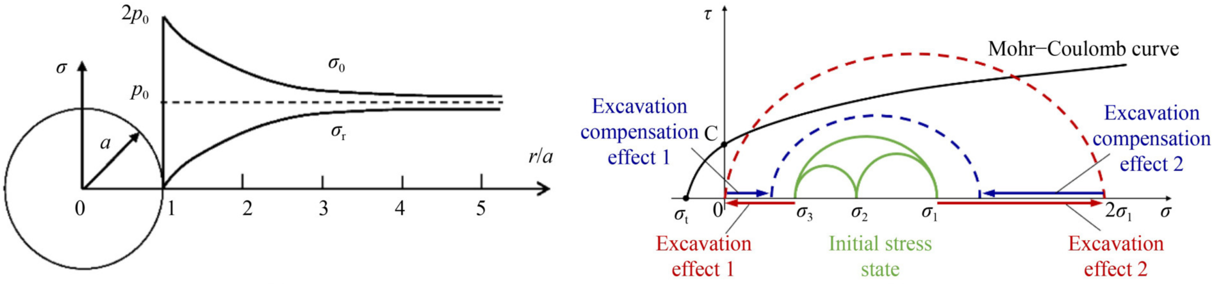

(a) (b)

Fig. 2 Excavation and compensation effect: (a) stress concentration phenomenon in excavations based on elastic mechanics; (b) different stages of the excavation compensation theory.

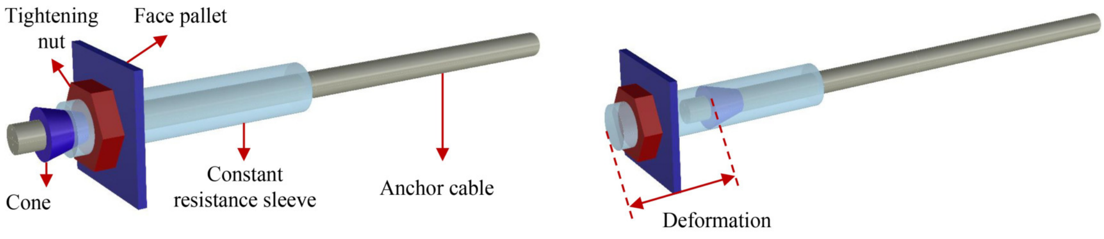

(a) (b)

Fig. 3 NPR anchor cable structure diagram: (a) initial state of NPR anchor cable; (b) constant resistance large deformation state of NPR anchor cable.

radial shrinkage and fracture. Consequently, the prestress design value for Positive Poisson's Ratio anchors is generally set at a lower range, approximately 30% to 50% of the yield strength. In contrast, NPR anchors can attain prestresses ranging from 80% to 90% of the yield strength [33]. In geological conditions characterized by minimal rock deformation following tunnel excavation, standard anchors can effectively suspend and interconnect loose rock blocks with the stable and solid rock outside the loosened region, thus averting potential dislodgement. Conversely, in more demanding geological settings where tunnel excavation induces substantial rock deformation, conventional anchors may prove inadequate in terms of deformation capacity to suspend and support the rock mass adequately. In such instances, NPR anchors, with their notable capability to undergo significant slippage, exhibit adaptability to rock mass deformation, ensuring the maintenance of a consistent and high level of resistance (Fig. 4).

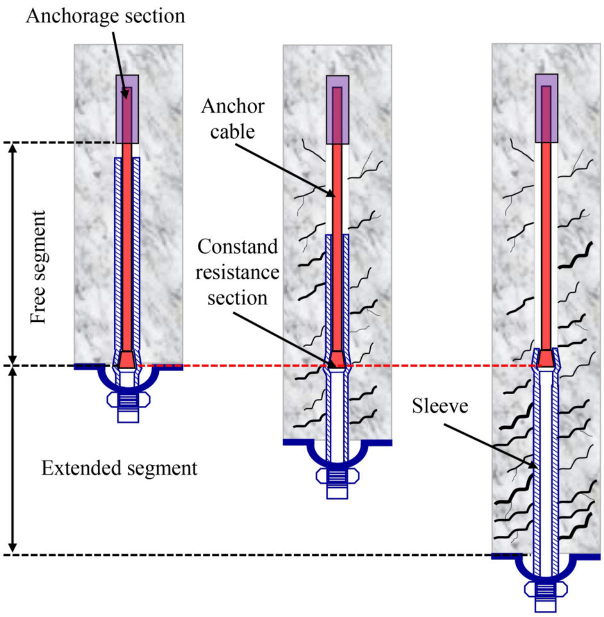

Fig. 4 1G-NPR anchor cable support principle.

3 Geomechanical model experiment

3.1 Similar simulation parameter design and material test

3.1.1 Parameter test of the granite and simulation material

This study is centered on the intersecting section where the Qiaocheng East Road mainline tunnel intersects with the Baopeng Passage. The tunnel possesses a three-centered arch shape, with the upper tunnel excavation featuring a span of 16.6 m and an excavation area of 159 m^2. The lower tunnel excavation spans 12 m with an excavation area of 95 m^2. This section presents intricate geological conditions, including a tunnel depth of 60 m and surrounding rock quality ranging from Grade IV to V. The overlying rock layers are threefold, arranged from top to bottom: loose-fill soil, moderately weathered medium-grained granite, and slightly weathered medium-grained granite.

Following the principles of similarity and utilizing Buckingham's π theorem, the fundamental parameters, including geometric dimensions (L), elastic modulus (E), Poisson's ratio (μ), density (γ), cohesion (c), stress (σ), and internal friction angle (φ), were calculated, as presented in Table 3. After reviewing pertinent literature, the materials selected for preparation were river sand, barite powder, gypsum, and water. Each sample underwent indoor uniaxial compressive strength tests, yielding uniaxial compressive strength curves (Fig. 5). Eventually, the material mixtures and their physical-mechanical parameters were determined, as detailed in Table 4.

Table 3 Similarity coefficient

Physical quantity	Similarity indicator	Similarity ratio
Length, L	C_L	50
Elastic modulus, E	C_E	70
Density, γ	C_γ	1.4
Stress, σ	C_σ	70
Internal friction angle, φ	C_φ	1

3.1.2 Experiment on the mechanical properties of the Negative Poisson's Ratio simulated materials

The miniature NPR anchor structure was replicated using a three-dimensional printing technique. The constant resistance of the NPR anchor cable relies on the frictional interaction between the constant resistance sleeve and the constant resistance body. This predetermined constant resistance was achieved during testing by adjusting the dimensions of the sleeve and the constant resistance body. Subsequently, a tensile test was conducted on the scaled NPR anchor cable specimen, and the corresponding curve is depicted in Fig. 6(b). The test results indicated that the average constant resistance of the specimen was 2.2 N, with an average elongation of 30.5 mm. These findings closely approximated the expected design values.

3.2 Principle of the experimental system and the monitoring equipment

The three-dimensional model test system (Fig. 7) was designed to consider boundary effects on both the front and sides of the intersecting tunnels simultaneously. The model device measured 1.6 m × 1.6 m × 1.6 m (height × width × thickness) and was primarily constructed from

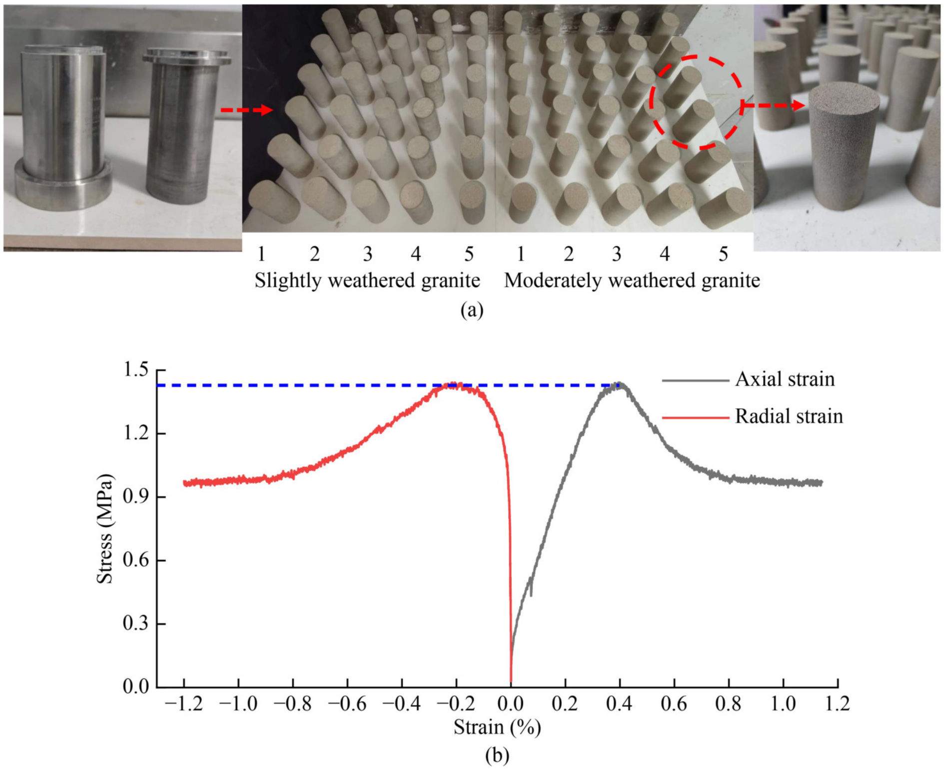

(a)

(b)

Fig. 5 Uniaxial compressive strength experiments on the simulated materials: (a) standard rock sample made of similar materials; (b) the obtained typical stress–strain curves.

Table 4 Ratio (mass) of similar simulated materials for the surrounding rock

Rock and soil type	River sand (%)	Gypsum (%)	Barite powder (%)	Water (%)	γ (kN·m^{-3})	σ_c (MPa)	E (GPa)
Natural soil	80	10	–	10	13.28	–	1.53×10^{-4}
Weathered granite	70	9	10	11	18.43	0.363	9.86×10^{-2}
Slightly weathered granite	55	17	20	8	19.14	1.31	0.398

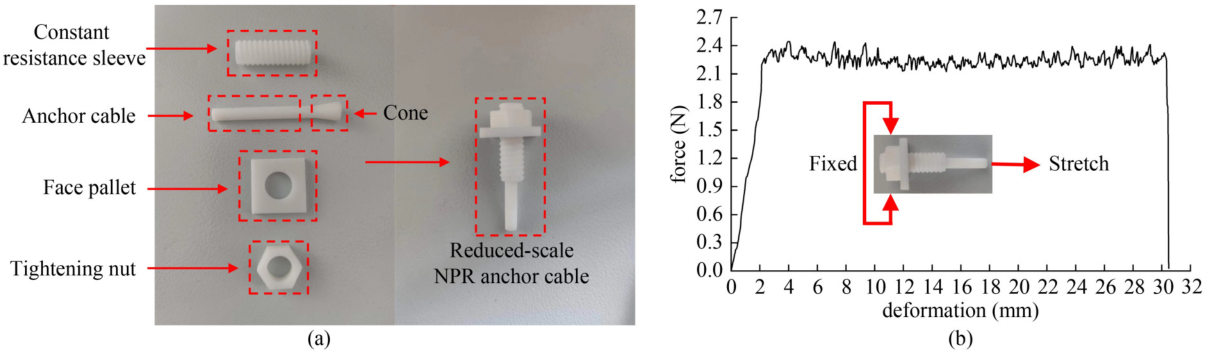

(a)

(b)

Fig. 6 Reduced-scale 1G-NPR anchor cable: (a) disassembly diagram; (b) tension–elongation diagram.

high-strength steel and steel plates. This system was primarily used for conducting three-dimensional tunnel model tests, with excavation windows set in the front, rear, left, and right directions to facilitate tunnel excavation and support work. Specifically, the upper tunnel had an excavation span of 32 cm and an excavation height of 23 cm, while the lower tunnel had an excavation span of 24 cm and an excavation height of 16 cm.

In the construction of intersecting tunnels, it is a common practice to first complete the lower tunnel before commencing work on the upper tunnel. While this sequential approach ensures construction quality, it may adversely impact construction progress. To address this challenge, load transfer beams were installed at the intersection points, enabling the upper and lower tunnels to converge at the crossing point (Fig. 8). This

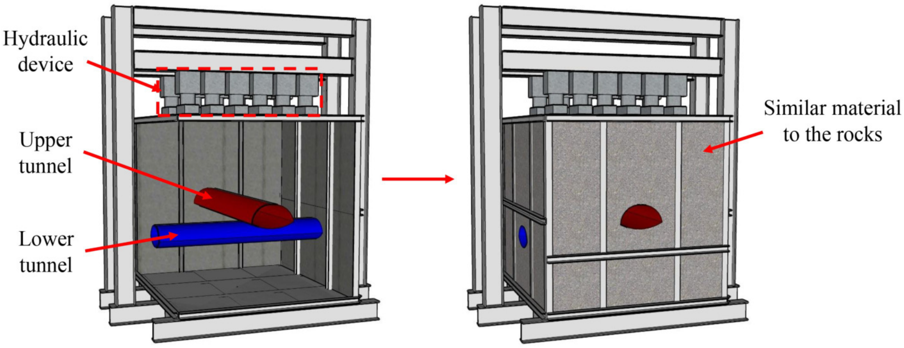

Fig. 7 Framework of the model test.

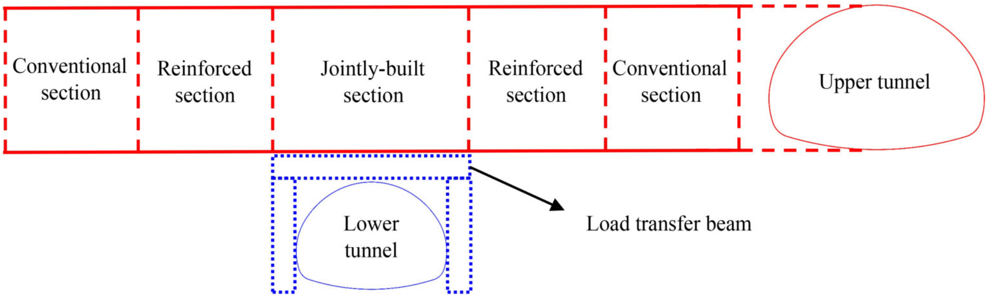

Fig. 8 Schematic diagram of the jointly built structure.

transformation essentially turns the bottom of the upper tunnel into the top of the lower tunnel, bolstering the structural integrity of the intersection. In the concurrent construction structure design, reinforcement sections were incorporated near the intersection to ensure the overall tunnel's safety. In this experiment, this specific area is referred to as the NPR anchor support zone and was constructed using high-strength concrete.

Both tunnels have a length of 1.6 m. However, conducting direct excavation within the model could potentially result in challenges such as tunnel misalignment and dimensional variations. To mitigate these issues and to facilitate more precise monitoring of tunnel deformation, aluminum sheets were utilized to construct tunnel profiles, with pre-fabricated anchor holes within them. In the case of the concurrent construction structure, aluminum sheets were employed to replicate the load transfer beams connecting the upper and lower tunnels, as illustrated in Fig. 9. Additionally, aluminum plates can also be used as similar materials for the initial support of tunnels. The parameters of materials are shown in Table 5.

Figure 10(a) illustrates the monitoring of anchor axial forces. Three-ring anchors were installed on both sides of the combined tunnel area within the reinforcement zone of both tunnels. These anchors were spaced 20 cm apart. In the upper tunnel, the axial forces of rings A1 and A2 were meticulously monitored, whereas in the lower tunnel, the axial forces of rings B1 and B2 were the focus of attention.

Figure 10(b) depicts the displacement monitoring surfaces. In this experiment, displacement sensors were deployed to track the movement of the surrounding rock in both the upper and lower tunnels. Five monitoring sections were established along the surrounding rock of both tunnels, and these sections were amalgamated to form a comprehensive tunnel surrounding rock displacement monitoring system.

Figure 10(c) illustrates the spatial arrangement of tunnel strain gauges. Strain gauges were employed to observe variations in tunnel strain on the aluminum tunnel model during the experiment. Within both the upper and lower tunnels, two circular strain monitoring sections were positioned, with each section monitoring

Fig. 9 The model of the collaborative construction structure.

Table 5 Parameters of the initial support material

Material	Thickness, *h* (mm)	Poisson's ratio, μ	Elasticity modulus, *E* (GPa)
High strength reinforced concrete	200	0.20	39
Similar material	0.8	0.30	68

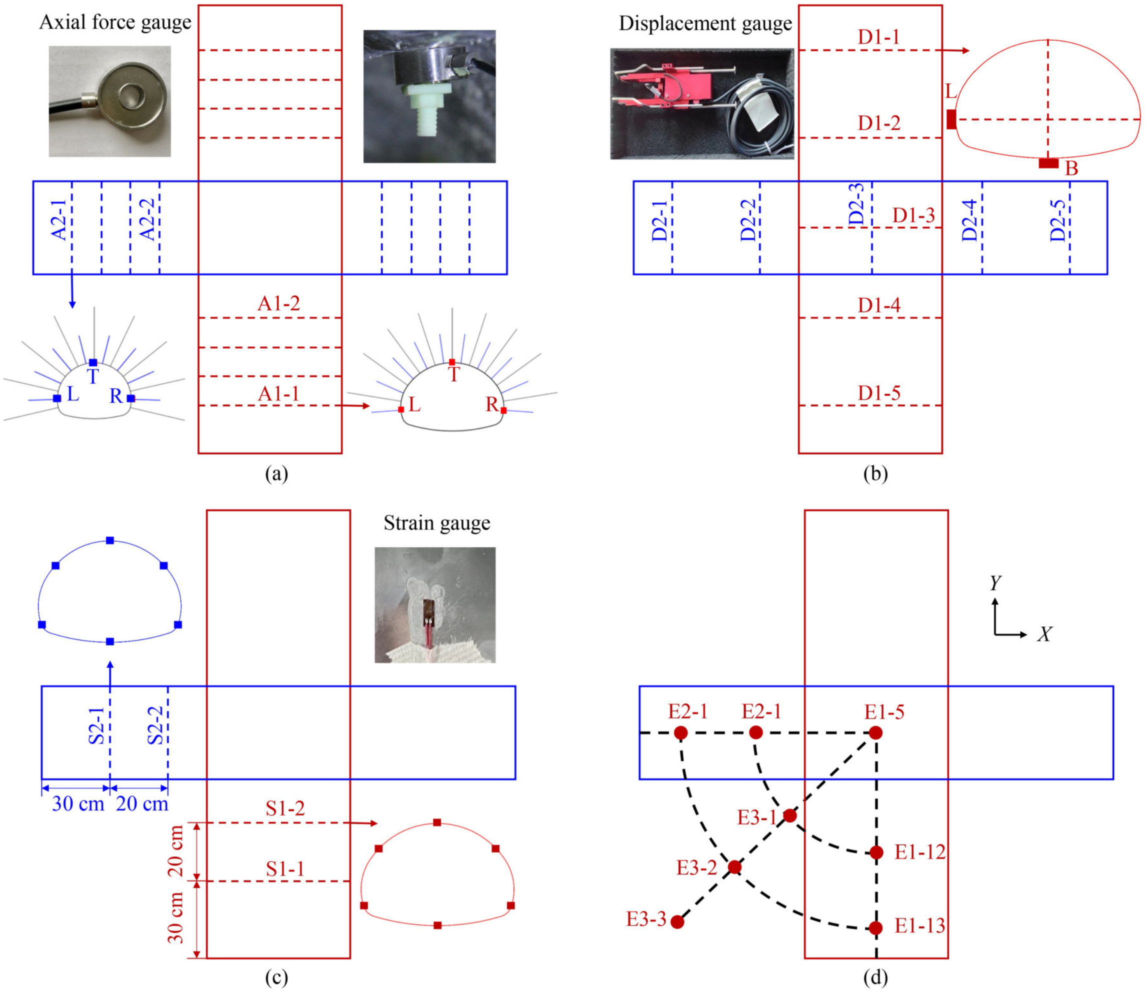

Fig. 10 Monitoring point layout: (a) axial force monitoring of anchor cables; (b) displacement monitoring; (c) tunnel strain monitoring; (d) earth pressure box monitoring.

six distinct points: the arch crown, left and right shoulders, left and right arch waists, and arch bottom. This resulted in a total of 24 strain gauges being utilized for strain monitoring.

Given the varying sizes of the upper and lower tunnel profiles and the differential distances of various tunnel sections from the combined construction structure, two-ring earth pressure monitoring sections were installed in both the large and small tunnels (Fig. 10(d)). These monitoring sections were spaced 20 cm apart to assess the impact of distinct tunnel sizes and combined construction structures on different tunnel sections.

3.3 Experimental scheme

The experiment is structured into three distinct stages.

Stage A. Involves simulating material compaction to the predetermined position and loading it to its initial stress state.

Stage B. Focuses on stabilizing the existing pressure, excavating the tunnel along the predefined excavation line, and subsequently increasing the anchoring after clearing debris.

Stage C. Encompasses the application of overloading stress to the model until the tunnel failure phenomenon is fully manifested.

As per the design of the combined construction structure, during the construction of intersecting tunnels, the excavation of the lower tunnel precedes the upper tunnel's breakthrough and support activities when construction reaches the intersecting section. This construction sequence is devised to minimize disruption to the surrounding rock. Therefore, the construction sequence for this experiment unfolds in two phases: the lower tunnel is constructed first until it approaches the intersecting area, at which point the upper tunnel's construction takes precedence. The specific construction sequence is visualized in Fig. 11.

4 Results

4.1 Macroscopic deformation characteristics

The entire loading process is segmented into three stages,

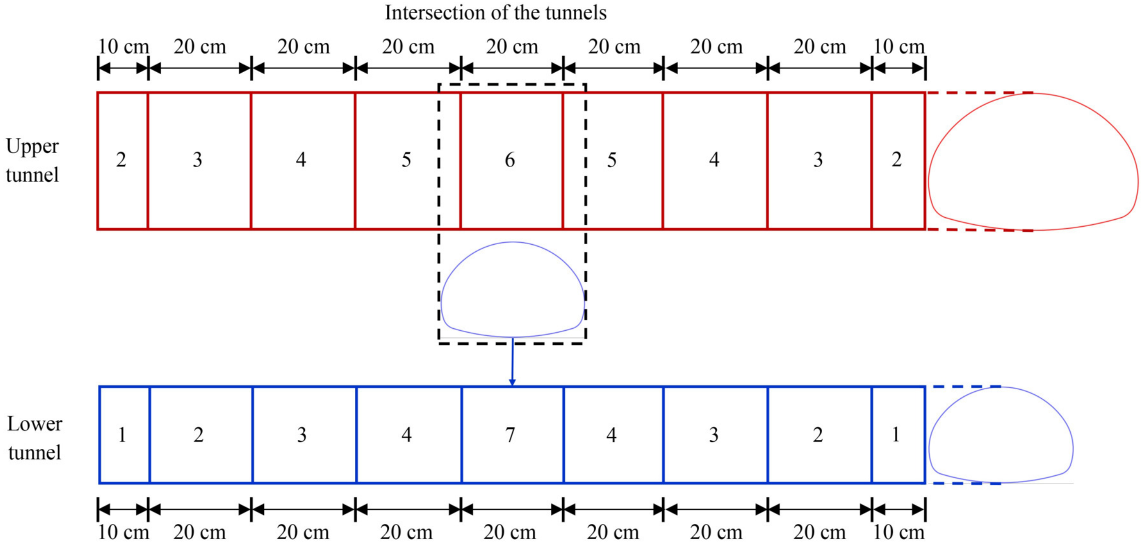

Fig. 11 Construction sequence of intersecting tunnel.

with each stage exhibiting distinct macroscopic failure characteristics, as depicted in Fig. 12.

Stage A (pre-loading stage). The model at stage A was preloaded so that it was compacted and kept stable for 20 min. At this time, there was no significant deformation of the tunnel and the surrounding rock remained stable. (Figs. 12(a) and 12(b)).

Stage B (excavation stage). The deformation of the tunnel during excavation in Stage B is presented in Figs. 12(c) and 12(d). Figures 12(c) and 12(d) represent the moments following the completion of excavation for the upper and lower tunnels, respectively. The subsidence of the vault in the combined area affected the reinforced section of the tunnel and promoted the slip phenomenon of the anchor cables. A subsidence of 9 mm occurred in the vault of the tunnel joint area, while the anchor cables in the tunnel reinforcement area showed multiple constant resistor slips of about 3 mm. When stress within the rock mass dissipates without adequate compensation, it leads to stress concentration within this zone and subsequent subsidence. The subsidence of the arch crown in the combined construction area has repercussions on the tunnel strengthening section, causing anchor slips. This observation underscores the significance of NPR anchors in compensating for sinking, as they demonstrate a “settlement but not collapsing” phenomenon in the tunnel strengthening area, showcasing the stabilizing effect of NPR anchors on subsiding areas. In contrast to the upper tunnel, the lower tunnel experiences less disturbance and exhibits no notable arch crown subsidence, with only minor deformation at the arch waist. This discrepancy is attributable to the presence of a load-transferring beam at the top of the combined construction area of the lower tunnel, reinforcing the support for the tunnel roof and preventing damage to the tunnel roof. From the failure observations, it is apparent that during the excavation process, there is a significant concentration of stress in the arch crown of the upper tunnel and the arch bottom of the lower tunnel. This concentration may result in arch crown subsidence and arch bottom uplift. However, in the overall context of Stage B, the surrounding rock of both the upper and lower tunnels remains relatively stable.

Stage C (overloading stage). Apply the overload pressure and record the deformation of the tunnel (Figs. 12(f) and 12(g)). Unlike the previous stage B, the deformation of the tunnel structure increases and evolves into a destructive phenomenon (Fig. 12(f)). The arch crown collapses by approximately 8 cm, and simultaneously, the surface surrounding rock forms a 15 cm collapsed arch. Additionally, multiple compression fractures develop on the right arch shoulder. In contrast, the surface surrounding rock of the lower tunnel exhibits minor erosion of rock and soil, accompanied by slight deformation of the tunnel profile. The primary tunnel structure remains essentially intact (Fig. 12(g)).

4.2 Surrounding rock displacement analysis

The three-dimensional fitting results of displacement monitoring surfaces following excavation completion are illustrated in Fig. 13. These surfaces provide insights into the deformation characteristics of distinct regions within the tunnel system.

Surface A. Corresponding to the displacement field of the upper tunnel’s crown surrounding rock, Surface A is influenced by the excavation of both the upper and lower tunnels. It demonstrates an overall sinking trend, with minimal displacement observed at the model’s coordinate origin, which is distant from the tunnel. However, the sinking trend becomes increasingly pronounced as it approaches the excavation contour of the tunnel, culminating in a maximum displacement value of 8.66 mm within the co-construction section.

Surface B. Positioned between the upper and lower

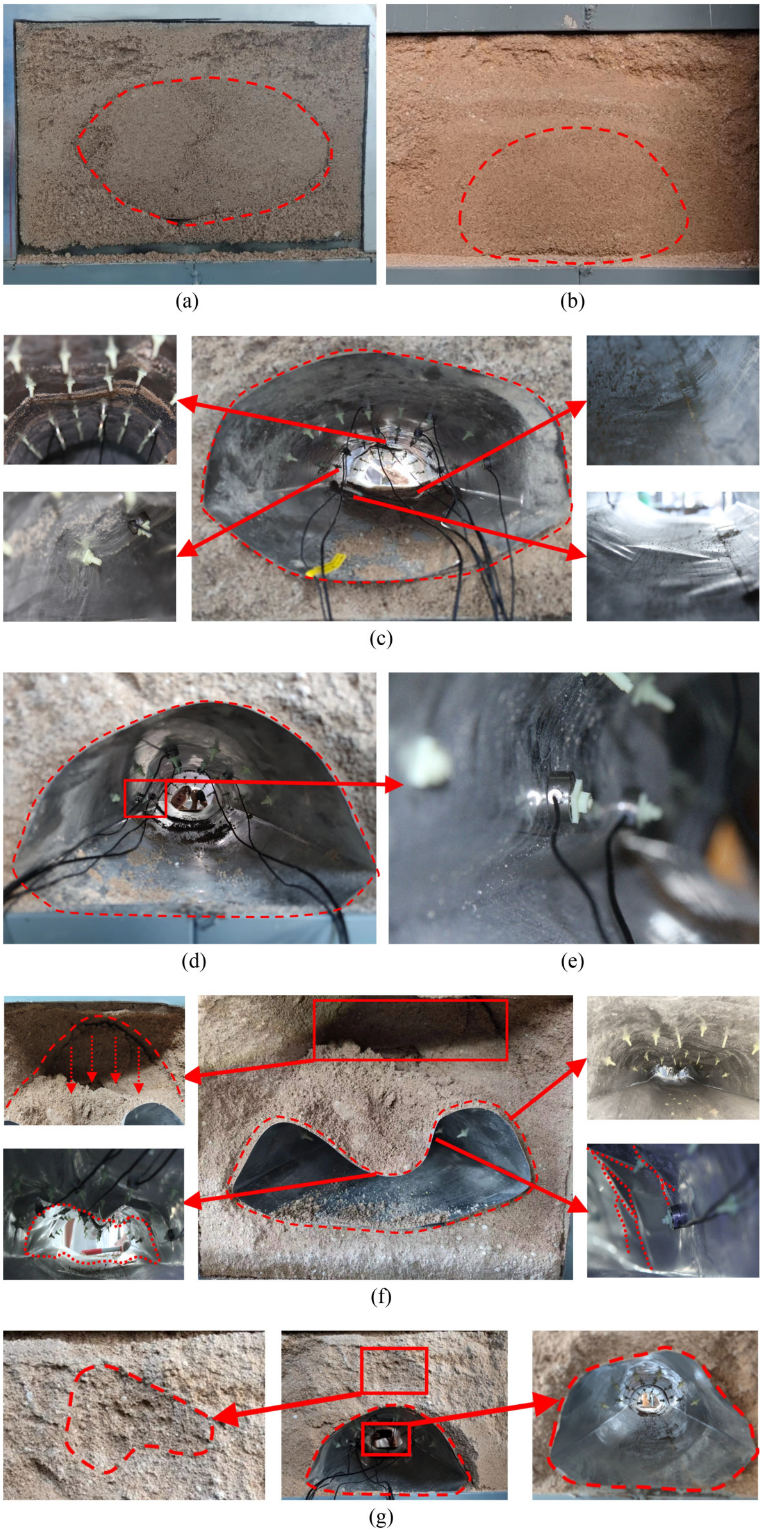

Fig. 12 Deformation process of the surrounding rock in the excavation stage: (a) upper tunnel Stage A; (b) lower tunnel Stage A; (c) upper tunnel Stage B; (d) lower tunnel Stage B; (e) tendency of arch rib contraction; (f) upper tunnel Stage C; (g) lower tunnel Stage C.

tunnels, Surface B is affected by both tunnels. The upper tunnel predominantly induces a bottom heaving effect on Surface B, while the lower tunnel primarily causes settlement. These two contrasting effects combine to create a 'saddle-shaped' displacement field. Specifically, the area near the excavation contour of the lower tunnel experiences slight bottom heaving, while the area near the excavation contour of the upper tunnel undergoes settlement. This displacement field possesses a complex form, but the absolute displacement values are relatively

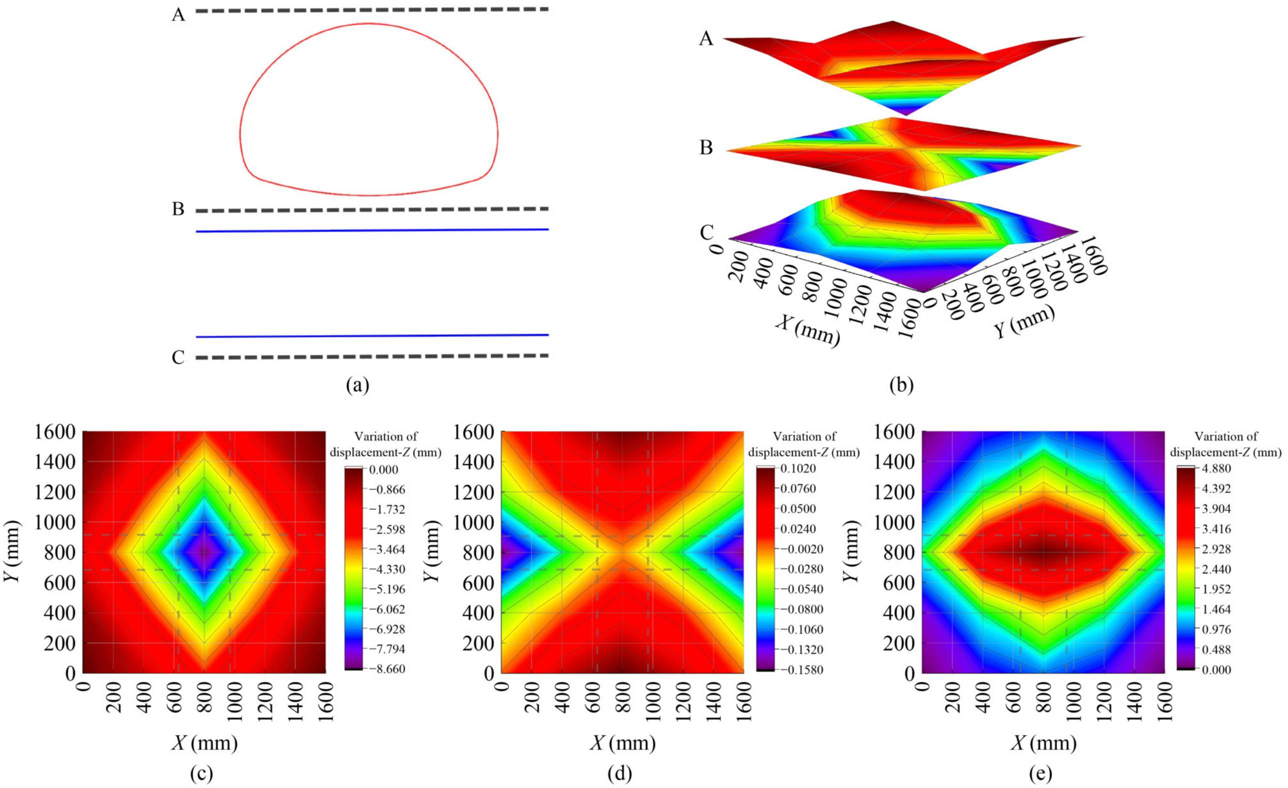

(a) (b)

(c) (d) (e)

Fig. 13 Displacement field of surrounding rock: (a) displacement monitoring surface; (b) displacement trend; (c) displacement cloud map of monitoring surface.

small, maintaining overall stability.

Surface C. This surface displays an overall rising trend, with the trend becoming more pronounced as it approaches the excavation contour of the lower tunnel. It reaches its maximum displacement value, ranging from 4.4 to 4.8 mm, at the invert of the lower tunnel.

4.3 Tunnel strain analysis

Figure 14 illustrates the strain behavior observed in various monitoring sections during the excavation process. These monitoring sections, located at different stages of construction, exhibit disturbance patterns that are not synchronized in time. Nevertheless, the overall trend follows a consistent pattern, which can be categorized into five stages: an initial minor disturbance stage near the monitoring surface, an intense disturbance stage during excavation up to the monitoring surface, a stress redistribution stage after passing the monitoring surface, a stable stage after moving away from the monitoring surface, and a stage of overall increased disturbance when the tunnel is fully excavated. The analysis reveals the following insights.

Varying degrees of excavation disturbance: While all four monitoring sections show a consistent trend, the extent of disturbance varies among them. During the excavation disturbance stage, the S2-1 section exhibits the smallest fluctuations, with approximately 50×10^{-6}, while the S2-2 monitoring section experiences around 80×10^{-6}. The S1-1 monitoring section records 120×10^{-6} of disturbance, and the S1-2 monitoring section exhibits the highest disturbance, with a strain increase of 180×10^{-6} during severe disturbance. Comparing the strain monitoring results at different sections of the same tunnel reveals that the disturbance at the 2nd monitoring section near the co-construction area is generally greater than that at the 1st section, indicating the presence of asymmetric forces in the axial direction of the tunnel. Furthermore, for different sections at the same monitoring location, such as S2-1 and S1-1, S2-2 and S1-2, the larger tunnel monitoring sections experience greater disturbance. This suggests that tunnels with larger excavation spans experience more significant disturbance under the same geological conditions and excavation sequence.

Minor fluctuations when tunnel is fully excavated: When the tunnel is fully excavated, all four monitoring sections exhibit minor fluctuations. This occurs because the co-construction structure connects the two tunnels as a single entity. During tunnel penetration, the central co-construction area experiences stress loss due to excavation without NPR anchor compensation. Consequently, the Mohr circle of the rock mass exceeds the Coulomb envelope, leading to deformation in the co-construction area, which affects the stabilized area already supported.

Stress redistribution stage at monitoring sections. As observed in the figure, when excavation reaches a

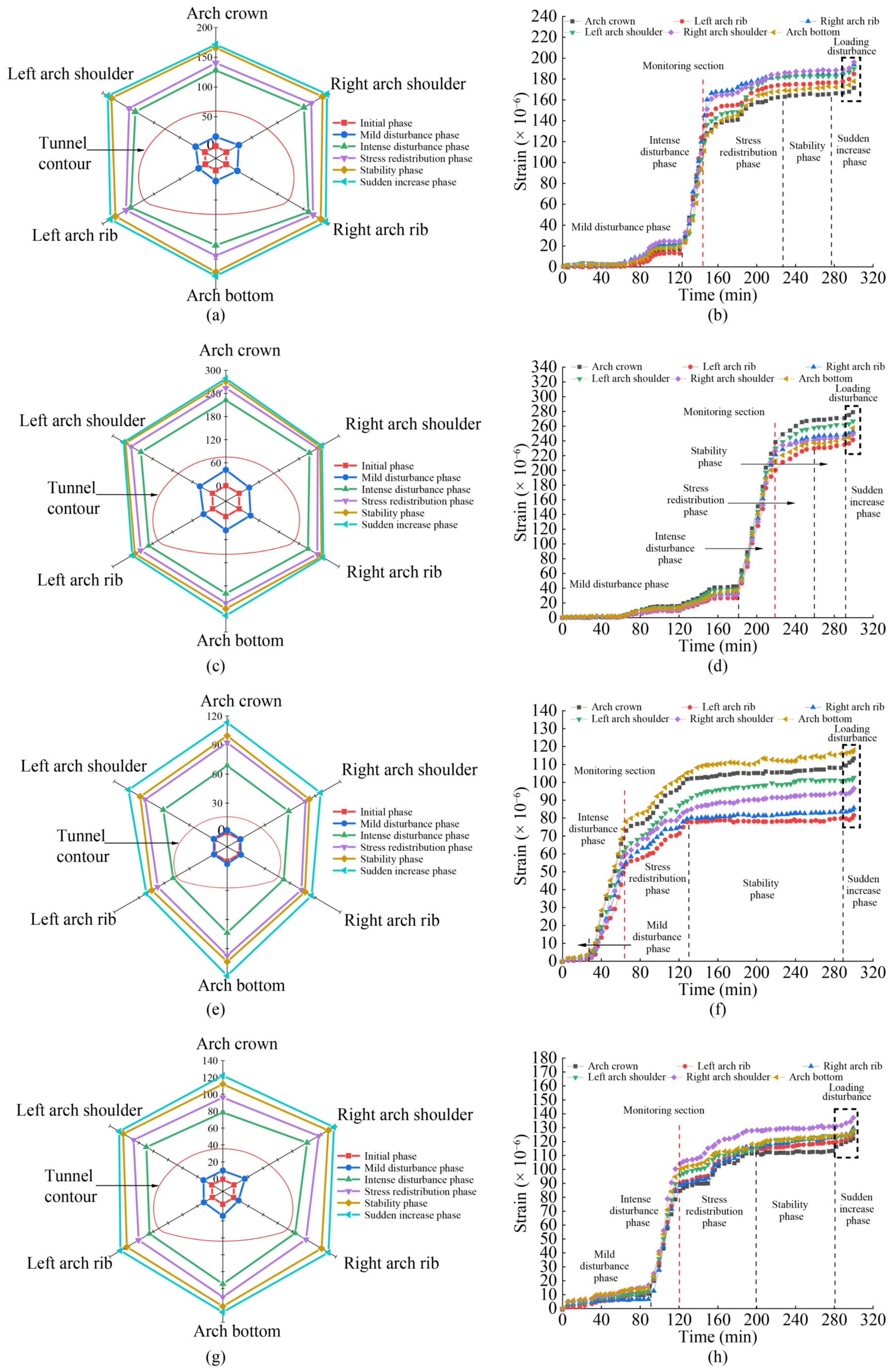

Fig. 14 Strain data of excavation process: (a) S1-1 radar chart; (b) S1-1 line chart; (c) S1-2 radar chart; (d) S1-2 line chart; (e) S2-1 radar chart; (f) S2-1 line chart; (g) S2-2 radar chart; (h) S2-2 line chart.

monitoring section, and if construction continues in other tunnel sections at that point, the monitoring section enters the stress redistribution stage. Subsequently, as excavation progresses away from the monitoring surface, disturbance continues but to a lesser extent. However, if excavation continues at the monitoring section after reaching it, the rock mass remains in a state of disturbance without undergoing the stress redistribution stage, resulting in a higher degree of disturbance.

4.4 Surrounding rock stress analysis

Figure 15 displays a three-dimensional fitted graph of the stress variation in the *Z*-direction of the surrounding rock in the tunnel intersection (earth pressure cells E1-1, E1-9, E1-10, E1-11). From the figure, the following observations can be made.

1) With the increase in excavation time, the stress at the intersection points initially increases and then decreases, with the inflection point occurring between 280 to 330 min. The reason for this phenomenon is that before the tunnels from both ends reach the intersection points, there is some stress concentration in the soil column at the intersection. As the excavation depth increases, this stress concentration intensifies, reaching a maximum of 1.94 kPa. Between 280 to 330 min, the lower small tunnel first breaks through, releasing the stress concentration. As a result, the stress in the surrounding rock at the lower monitoring points decreases earlier and at a slower rate, ultimately stabilizing at around 2 kPa. The upper large tunnel breaks through slightly later, so the stress release at the upper monitoring points occurs later and at a faster rate, stabilizing at around 4.5 kPa.

2) From a spatial perspective, due to the larger cross-section of the upper tunnel, the stress concentration is more severe in the upper part of the intersection, and the rate of stress change is also faster than in the lower part.

Figure 16 presents a three-dimensional fitted graph illustrating the normal stress in the *Z*-direction on the *X*−*Y* plane at the tunnel intersection (earth pressure cells E1-5, E3-1, E3-2, E3-3, with positive stress representing compression). Several observations can be drawn from the figure.

Excavation progress. Over time, there is a notable overall trend of increasing stress due to stress concentration in the intersecting section. During the alternating process of excavation and support, there is a cyclical pattern of stress increase and decrease. Ultimately, upon the completion of excavation, stress concentration reaches its maximum value of 5.34 kPa.

Spatial perspective. Concerning spatial distribution, as the distance from the monitoring points to the intersecting

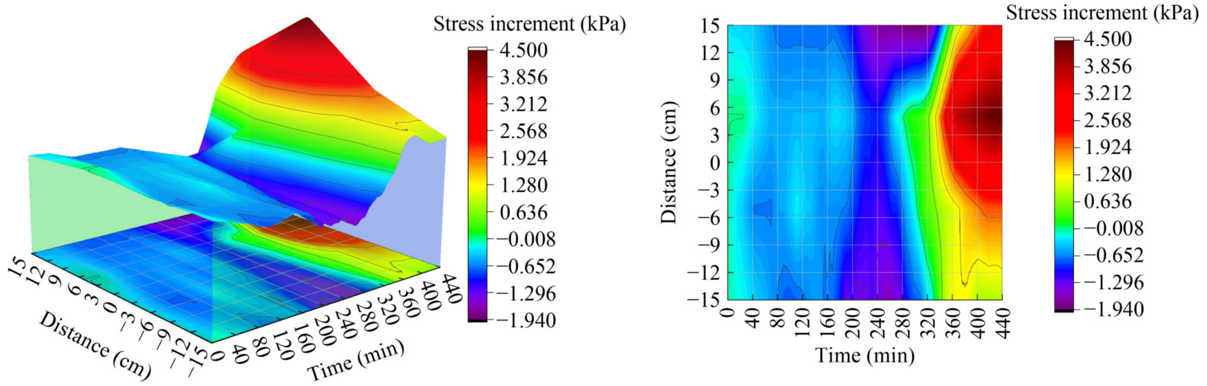

Fig. 15 *Z*-direction stress-*zz* field in intersection segment.

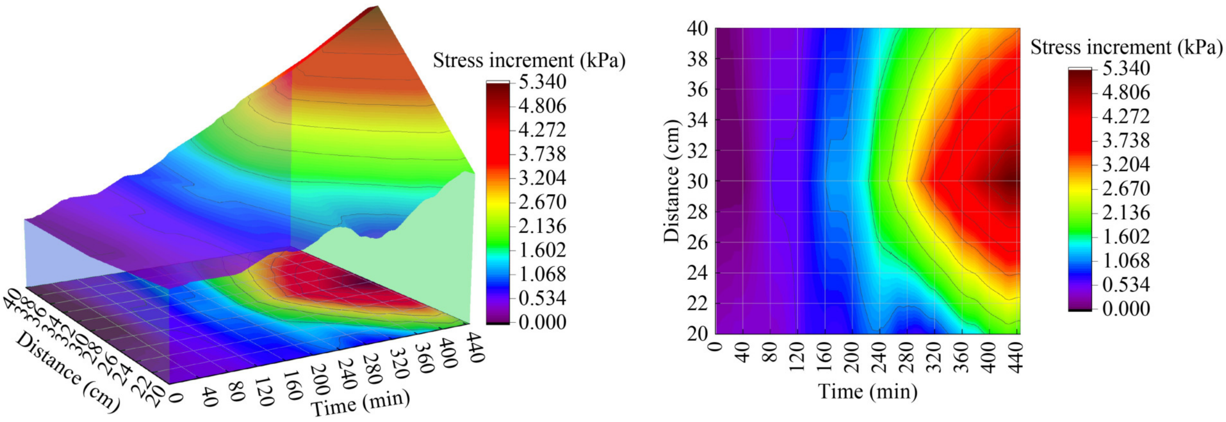

Fig. 16 Stress-*zz* field of intersecting section *X*−*Y*.

section increases, the stress exhibits an initial increase followed by a decrease. The maximum stress value of 5.34 kPa is observed at a point located 30 cm away from the intersecting section. This pattern arises because the influence range of the plastic zone on the X−Y plane extends up to 30 cm.

4.5 Anchor force analysis

The anchor force variation chart in Fig. 17 (anchor force monitoring surfaces A1-1, A1-2, A2-1, A2-2) provides several noteworthy observations.

1) Gradual increase in anchor force: After construction to the predetermined position and the installation of NPR anchors, the anchor force gradually begins to rise as the tunnel face continues to advance. When the face construction distance reaches approximately twice the tunnel diameter from the anchors, the anchor force stabilizes, and further significant changes are no longer observed.

2) Significant anchor force increase at intersection area: However, when the lower tunnel intersection area is excavated, and breakthrough occurs, there is a substantial overall increase in anchor forces. This increase indicates that the stress disturbance in the intersection area has a notable impact on the anchor forces along the entire tunnel. The right shoulder of A2-2 exhibits the highest axial force, reaching 2.41 N, and the axial forces of the entire A2-2 section surpass 2.2 N, suggesting that it has entered or is about to enter a constant resistance state.

3) Variation in anchor forces among sections: The left shoulder of A1-1 has the lowest axial force, measuring only 1.81 N, and the overall axial forces of the A1-1 section do not exceed 2.2 N. This implies that the A1-1 section experiences relatively minor disturbance and remains relatively stable. Comparing the anchor forces of different sections of the same tunnel (e.g., A1-1 and A1-2 sections), it is evident that the overall axial forces of the A1-2 section, which is closer to the intersection area, are greater than those of the A1-1 section. This indicates that the tunnel closer to the intersection area experiences more significant disturbance, resulting in an overall increase in axial forces.

5 Numerical simulation

5.1 Numerical model construction

In the numerical simulation model for the intersecting tunnels, the dimensions and characteristics of the tunnels are as follows (Fig. 18).

1) Overall model dimensions: length × width × height = 1.6 m × 1.6 m × 1.6 m.

2) Upper tunnel model (corresponding to Qiaocheng Tunnel): excavation span: 32 cm; excavation height: 23 cm.

3) Lower tunnel model (corresponding to Ramp): excavation span: 24 cm; excavation height: 16 cm.

The excavation and support methods employed in the numerical simulation model are consistent with those used in the physical model experiment. This ensures that the numerical simulation accurately replicates the conditions and behavior of the intersecting tunnels during excavation and support.

Throughout the calculation process, both an elastic model (isotropic elasticity model group) and a plastic model (Mohr–Coulomb model group) were utilized, with the following geomechanical parameters assigned to each stratum (Table 6).

5.2 Analysis of calculation results

Analyze the excavation process of the upper-level tunnel

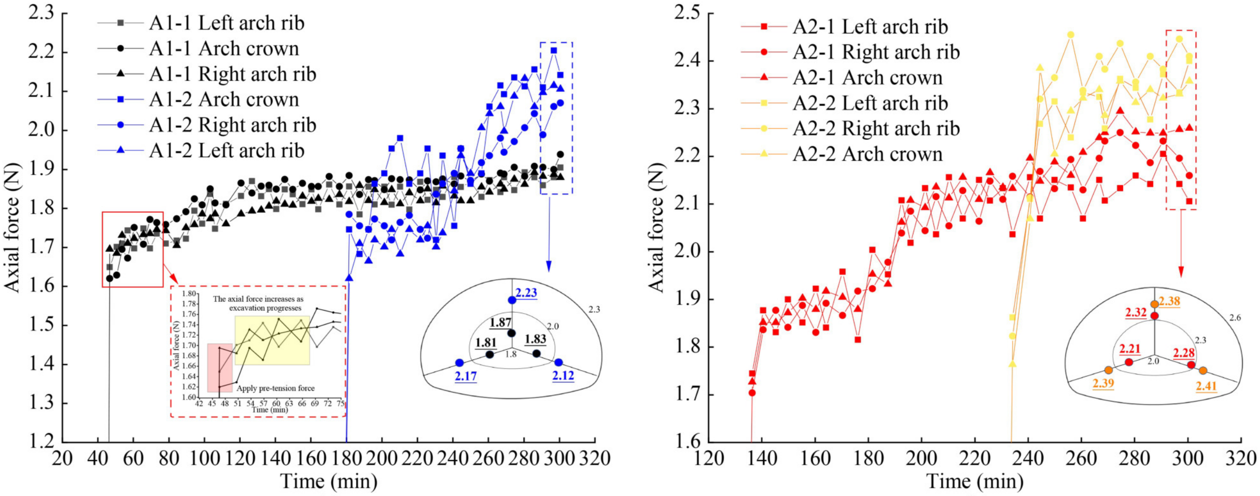

(a)

(b)

Fig. 17 Axial force of NPR anchor cable during excavation: (a) upper tunnel monitoring point; (b) lower tunnel monitoring point.

as illustrated in Fig. 19.

From the observation of the figure, several key points can be noted regarding the excavation process of the upper-level tunnel: Initially, when excavation began for the upper-level tunnel, significant displacement changes were observed, with the crown settling by approximately 4 mm, as shown in Fig. 19(a). Within the excavation range of 0.2 to 0.6 m, displacement increased relatively modestly, aided by the support of anchorages. After the complete excavation and breakthrough of the upper-level tunnel, the crown displacement increased to 5 mm, while the deformation at the tunnel's base reached 6.5 mm. The breakthrough of the lower-level tunnel resulted in a change in the displacement distribution of the upper-level tunnel. The crown displacement of the upper-level tunnel decreased, and the reduction in base displacement deformation became more pronounced, contributing to the stability of the upper-level tunnel.

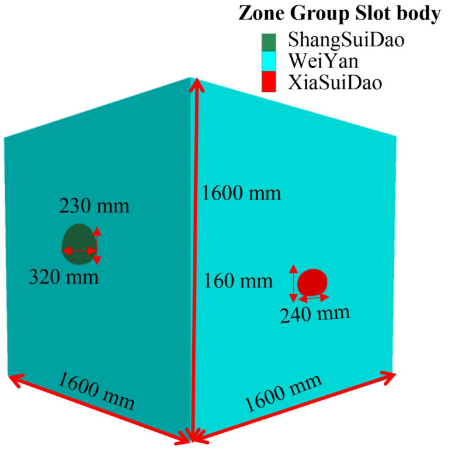

Fig. 18 Numerical simulation model size.

The breakthrough of the lower-level tunnel led to a significant increase in base displacement, reaching 7 mm. From the excavation process of the upper-level tunnel, the following observations can be made.

1) During the initial excavation phase of the upper-level tunnel, there was a notable displacement change. However, the increment in settlement reduced after excavation reached the NPR anchor support zone.

2) After the complete excavation of the upper-level tunnel, with its center section as the focal point, displacement gradually decreased outward.

3) The breakthrough of the lower-level tunnel impacted the displacement distribution of the upper-level tunnel,

Table 6 Physical and mechanical parameters of each rock layer in numerical simulation

Rock and soil type	Density (kN/m^3)	Young's modulus (GPa)	Poisson's ratio	Tensile strength (MPa)	Cohesive strength (kPa)	Friction angle (°)	Computational model
Natural soil	1350	1.47×10^{-4}	–	–	0.34	16	Mohr–Coulomb model
Weathered granite	1850	9.75×10^{-2}	0.24	0.367	48.27	31	Mohr–Coulomb model
Slightly weathered granite	1900	0.58	0.26	0.87	114.57	37	Mohr–Coulomb model
Lining	2700	70	0.3	–	–	–	elastic model

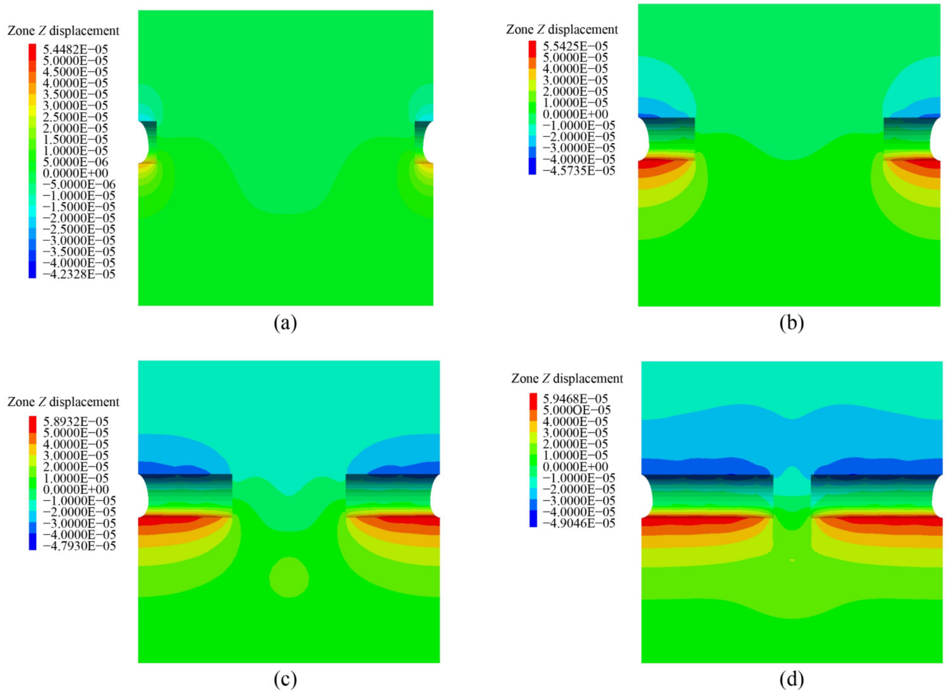

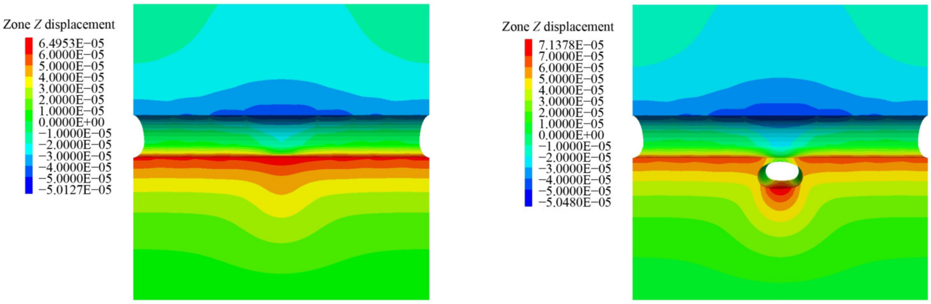

(e) (f)

Fig. 19 Vertical displacement of the upper tunnel during excavation: (a) excavation of the upper tunnel by 0.1 m; (b) excavation of the upper tunnel by 0.3 m; (c) excavation of the upper tunnel by 0.5 m; (d) excavation of the upper tunnel by 0.7 m; (e) the upper tunnel excavation has broken through; (f) the lower tunnel excavation has broken through.

resulting in reduced displacement changes at the crown and base of the upper-level tunnel. However, the base displacement change of the lower-level tunnel became significantly pronounced, representing the most critical area.

Analyzing the displacement of the lower-level tunnel during the excavation process reveals the following observations.

1) In the early stages of excavation for the lower-level tunnel, there was a significant displacement change, with the base settling by approximately 4 mm, as shown in Fig. 20(a). The increase in displacement was relatively minor when excavation reached the NPR anchor support zone.

2) The excavation breakthrough of the upper-level tunnel led to an increase in the displacement of the lower-level tunnel's base, particularly in the central base of the upper-level tunnel and the front area of the lower-level tunnel's invert. These regions exhibited the greatest base displacement.

3) The breakthrough of the lower-level tunnel during excavation had a notable impact on the overall displacement field, especially in the co-construction zone of the lower-level tunnel, where the base displacement was the greatest and exhibited a trend of bottom heaving. This observation is consistent with the results observed in the physical model experiments.

An analysis of the surrounding rock stress field during tunnel excavation reveals the following observations from the figure.

1) When the tunnel was initially excavated, the stress on the crown and invert of the lower-level tunnel, as well as at the tunnel face, was relatively high, as depicted in Fig. 21(a).

2) As tunnel excavation progressed, the maximum principal stress gradually increased, with the stress in the lower-level tunnel exceeding that in the upper-level tunnel. Before the tunnel breakthrough, the maximum principal stress was located at the crown and invert of the lower-level tunnel.

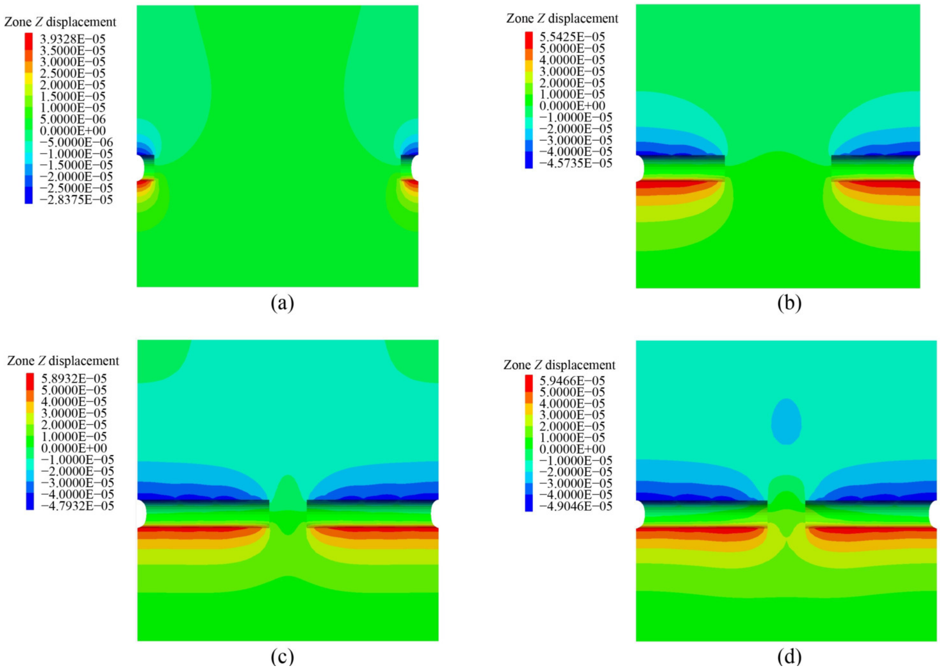

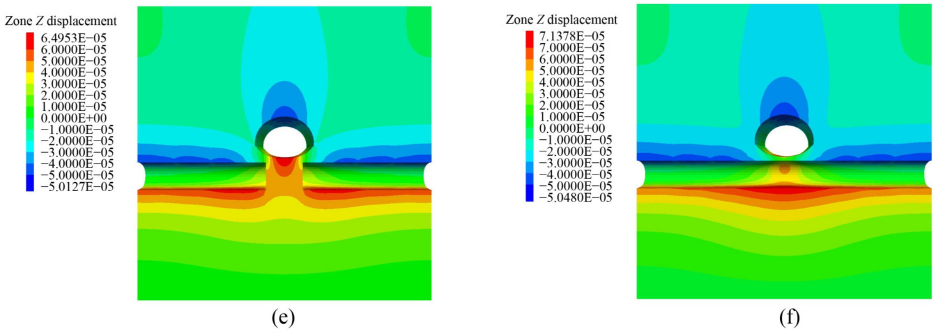

Fig. 20 Change of vertical displacement of the lower tunnel during excavation: (a) excavate the lower tunnel by 0.1 m; (b) excavate the lower tunnel by 0.5 m; (c) excavate the lower tunnel by 0.1 m; (d) excavation of the upper tunnel by 0.7 m; (e) the upper tunnel excavation has broken through; (f) the lower tunnel excavation has broken through.

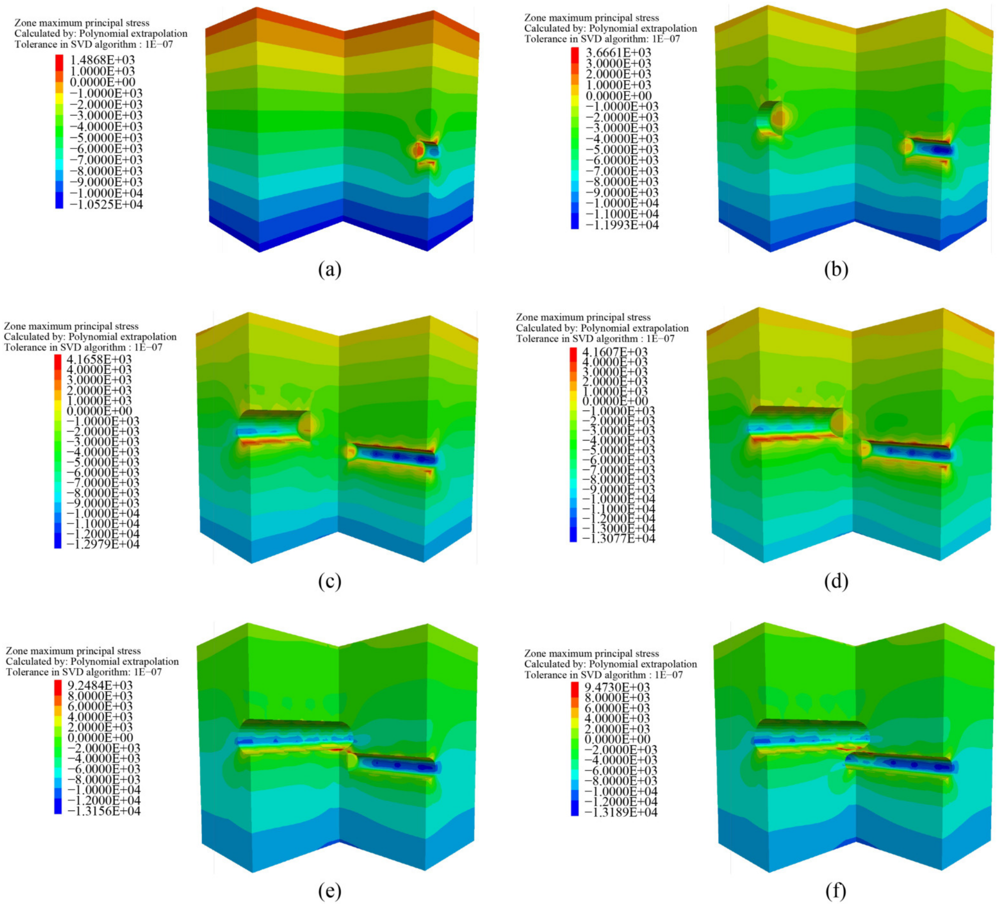

Fig. 21 Stress field analysis during tunnel excavation process: (a) excavate the lower tunnel by 0.1 m; (b) excavate the upper tunnel by 0.1 m; (c) excavate the upper tunnel by 0.5 m; (d) excavate the upper tunnel by 0.7 m; (e) the upper tunnel excavation has broken through; (f) the lower tunnel excavation has broken through.

3) When the upper-level tunnel breakthrough occurred, elevated stress levels were observed at the crown of the upper-level tunnel and in the connecting area between the upper and lower tunnels. After the lower-level tunnel breakthrough, significant stress was experienced at the load transfer beam. This observation is consistent with the results observed in the physical model experiments.

6 Conclusions

The study takes the joint structural section of Shenzhen Nanlong Interchange Tunnel as the experimental background, and carries out the physical modeling experiments and numerical simulation study of the intersecting section of the interchange tunnel under the support of NPR anchors based on the theory of compensated excavation. The following conclusions are obtained through the study of tunnel surrounding rock under excavation support and overload condition.

1) The test results show that in the tunnel excavation and support stage, the surrounding rock disturbance of the tunnel will increase with the increase of the tunnel excavation span; when the tunnel is excavated through, since the stress in the joint area is not compensated, the stress will spread to the surrounding area, generating a stress wave spreading from the joint area to the surrounding area. In terms of displacement, with the intersecting section as the center, the upper peripheral rock has a tendency to settle, and the lower peripheral rock has a tendency to rise, and the superposition of the upper and lower displacement fields forms a "saddle-shaped" displacement field at the intersection of the two tunnels. In the numerical simulation, after loading, the displacement shows a cone shape, pointing to the joint construction area from big to small. The simulation is in agreement with the test results.

2) The damage mechanism of the intersecting tunnels under "excavation-overloading" condition is derived. The damage process is divided into 2 stages.

2a) Upper tunnel deformation stage. The main feature of this stage is that the roof of the upper tunnel deforms seriously but the lower tunnel does not change much. The overload stress is transmitted from the upper to the lower level, which first deforms the tunnel vault.

2b) Lower tunnel deformation stage. The main feature of this stage is that the upper tunnel vault is transformed from local collapse to large-scale collapse, and the bottom drum of the lower tunnel is more developed. Different from the previous stage, the deformation of the lower tunnel can be obviously observed. At the same time, the deformation of the lower tunnel also contributes to the large-scale spalling of the surrounding rock on the tunnel surface.

3) The role of NPR anchors in supporting intersecting tunnels has been revealed. It is found that the high stress compensation characteristic of NPR anchors can resist the settlement of the support area. Under this system, the NPR anchor cable can cope with the disturbance in the normal condition. However, when overloaded, the stress concentration in the arch leads to damage in the tunnel reinforcement area, which can be effectively solved by NPR anchor cable support in the upper tunnel joint area during subsequent construction.

Acknowledgements The authors acknowledge financial support from the National Natural Science Foundation of China (Grant No. 42377154).

Competing interests The authors declare that they have no competing interests.

References

1. Chen W J, Zhu Z L. A review on the technology used in closely overlapped tunnels. Modern Tunnelling Technology, 2002, 1: 42–47 (in Chinese)
2. Li Z P, Wang T, Zheng H, Mo C J, Nie N. Option for a shield tunnel driving across above an existing bored tunnel in close proximity with a small intersection angle. Urban Rapid Rail Transit, 2008, 21: 64–68 (in Chinese)
3. Zhang M Q. Feasibility study of bored driving from Luohu Station to Dajuyuan Station in Shenzhen Subway. World Tunnelling, 1999, 3: 1–7 (in Chinese)
4. Wang L, Jiang D Y, Ren S. Construction technology of cross tunnel with small interval. Communications Standardization, 2008, 9: 23–27 (in Chinese)
5. Chen H X, Wu M S. The key points of the Jiahua Tunnel's vertical intersection section design. Modern Tunnelling Technology, 2008, 45: 337–342 (in Chinese)
6. Han X J. Vertical intersection excavation and support construction techniques for new and existing tunnels. Railway Standard Design, 2000, 8: 46–47 (in Chinese)
7. Chen G. Construction technology on three-dimensional intersection section for subbottom tunnel. Railway Construction Technology, 2015, S1: 189–191 (in Chinese)
8. Ye Z S, Yang F M. Case study on integration of municipal tunnel and metro station. Tunnel Construction, 2015, 35: 1301–1305 (in Chinese)
9. He Z H. Design and analysis of a municipal tunnel intersecting with a rail transit tunnel. Soil Engineering and Foundation, 2019, 33: 285–289 (in Chinese)
10. Cheng Y. The influence of intersecting tunnel construction grouting parameters of shield tail on ground surface settlement. Journal of Tongling University, 2018, 17: 93–96 (in Chinese)
11. Luo Z X, Zhang M C, Zhong Z L. Study on the influence of blasting construction of space cross tunnel on adjacent tunnel. Chinese Journal of Underground Space and Engineering, 2018, 14: 205–213 (in Chinese)
12. Wang Z C, Jiang X F, Li Y Z. Numerical simulation of deformation laws of surrounding rock at the intersection of bifurcate tunnel. Journal of Liaoning Technical University (Natural Science), 2017, 36: 598–603 (in Chinese)
13. Wang Y, He C, Zeng D Y, Su Z X. Model test and numerical simulation of influence of perpendicular undercross shield tunnel construction on existing tunnel. Journal of the China Railway Society, 2010, 32: 79–85 (in Chinese)
14. Li S G, Liu B G. Study on the zero distance excavation technology of deep buried perpendicular tunnel. Journal of Beijing Jiaotong University, 2010, 34: 36–40 (in Chinese)
15. Xu J W. Impact of perpendicular undercrossing tunneling construction on existing tunnel. Subgrade Engineering, 2017, 1: 169–173 (in Chinese)
16. Meguid M A, Rowe R K. Stability of D-shaped tunnels in a Mohr–Coulomb material under anisotropic stress conditions. Canadian Geotechnical Journal, 2006, 43(3): 273–281
17. Zhang C, Feng X T, Zhou H. Estimation of *in situ* stress along deep tunnels buried in complex geological conditions. International Journal of Rock Mechanics and Mining Sciences, 2012, 52: 139–162
18. Fu Q, Yang J, Gao Y, Li C, Song H, Liu Y, Wu X. Combined

blasting for protection of gob-side roadway with thick and hard roof. Journal of Rock Mechanics and Geotechnical Engineering, 2024, 16(8): 3165–3180

19. He M, Sui Q, Li M, Wang Z, Tao Z. Compensation excavation method control for large deformation disaster of mountain soft rock tunnel. International Journal of Mining Science and Technology, 2022, 32(5): 951–963
20. Li G, Zhu C, Hongliang L, Tang S, Du K, Wu C Z. Energy balance support method in soft rock tunnel with energy absorbing anchor cable. Tunnelling and Underground Space Technology, 2023, 141: 105380
21. Tao Z G, Li H X, Cao H, Pang S H, Wang H. Test on the slope stability of full-section high dump under rainfall. Journal of China Coal Society, 2020, 45: 3793–3805 (in Chinese)
22. Wang F N, Guo Z B, Qiao X B, Fan J Y, Li W, Mi M, Tao Z G, He M C. Large deformation mechanism of thin-layered carbonaceous slate and energy coupling support technology of NPR anchor cable in Minxian Tunnel: A case study. Tunnelling and Underground Space Technology, 2021, 117: 104151
23. Sun X, Zhang B, Yang K, Guo P, Tao Z. Large deformation mechanism of foliated rock and NPR anchor cable support technology in the Changning Tunnel: A case study. Rock Mechanics and Rock Engineering, 2022, 55(11): 7243–7268
24. He M, Ren S, Guo L, Lin W, Zhang T, Tao Z. Experimental study on influence of host rock strength on shear performance of micro-NPR steel bolted rock joints. International Journal of Rock Mechanics and Mining Sciences, 2022, 159: 105236
25. He M, Gong W, Wang J, Qi P, Tao Z, Du S, Peng Y. Development of a novel energy-absorbing bolt with extraordinarily large elongation and constant resistance. International Journal of Rock Mechanics and Mining Sciences, 2014, 67: 29–42
26. Hao L, Gong W, He M, Song Y, Wang J. Dynamic model and mechanical properties of the two parallel-connected CRLD bolts verified with the impact tensile test. Mathematical Problems in Engineering, 2018, 2018: 1–17
27. Li Z, Lv Q, Zhu H, Hu J, Feng J, He M. Laboratory testing and modeling of a high-displacement cable bolt. International Journal of Geomechanics, 2019, 19(7): 04019078
28. Li G, Zhu C, He M, Zuo Y, Gong F, Xue Y, Feng G. Intelligent method for parameters optimization of cable in soft rock tunnel base on longitudinal wave velocity. Tunnelling and Underground Space Technology, 2023, 133: 104905
29. Li G, Tao Z G, Sun X M, Zhu C. Study on the method of roadway cooperative anchor support based on rock mass safety factor. Chinese Journal of Rock Mechanics and Engineering, 2023, 42(6): 1395–1404 (in Chinese)
30. Zhu C, He M, Jiang B, Qin X, Yin Q, Zhou Y. Numerical investigation on the fatigue failure characteristics of water-bearing sandstone under cyclic loading. Journal of Mountain Science, 2021, 18(12): 3348–3365
31. He M, Sui Q, Li M, Wang Z, Tao Z. Compensation excavation method control for large deformation disaster of mountain soft rock tunnel. International Journal of Mining Science and Technology, 2022, 32: 951–963
32. He M, Li C, Gong W, Sousa L R, Li S. Dynamic tests for a constant-resistance-large-deformation bolt using a modified SHTB system. Tunnelling and Underground Space Technology, 2017, 64: 103–116
33. Sui Q, He M, He P, Xia M, Tao Z. State of the art review of the large deformation rock bolts. Underground Space, 2022, 7(3): 465–482